RESEARCH ARTICLE

Check for updates

Regulating the microscopic structure of solutions to synthesize centimeter-sized low-dimensional $Cs_mSb_nCl_{m+3n}$ perovskite single crystals for visible-blind ultraviolet photodetectors†

Wenzhen Wang, [ID] [a,b,d] Shanhu Xu,[a] Ziyi Lai,[a] Xiaoxi Feng,[a] Huanzhen Qi,[a] Qiutao Pan,[a] Zichen Yang,[c] Jiaxing Kang,[c] Yue Li,[c] Xin Shu,[c] Zifa Zhang,[c] Yan Zhu,[d] Jiaxin Bai,[e] Feng Hong, [ID] [c] Juan Qin,[b] Run Xu, [ID] *[a,b] Ying He,[c] Fei Xu[c] and Linjun Wang[a,b,c]

Chlorine-based all-inorganic lead-free halide perovskites exhibit excellent properties in visible-blind ultraviolet detectors. However, the quality and size of these solution-grown single crystals are still far from meeting commercial standards due to their low solubility, and a fundamental understanding of the underlying causes of low solubility is still lacking. Herein, the effects of the microscopic structure of solutions on the solubility have been systematically investigated, and it has been demonstrated that a hybrid solvent consisting of dimethyl sulfoxide and hydrochloric acid can significantly improve the solubility of the raw materials of $Cs_mSb_nCl_{m+3n}$ ($SbCl_3$ and $CsCl$). Centimeter-sized high-quality α-$Cs_3Sb_2Cl_9$ and $Cs_5Sb_2Cl_{11}$ single crystals are grown by the effective hybrid solvent. The low dark current density (91 pA cm^{-2}), excellent wavelength selectivity ($R_{360}/R_{480} = 150$), and fast response speed ($t_r = 21.7$ ms, $t_d = 104.4$ ms) of the photodetector based on the Au/α-$Cs_3Sb_2Cl_9$/Au structure powerfully demonstrate the great potential of $Cs_mSb_nCl_{m+3n}$ in ultraviolet applications. Furthermore, the method of using hybrid solvents to increase solubility can be extended to the growth of all inorganic chloride perovskite single crystals, thereby driving the exploration of their future optoelectronic applications.

[a]*School of Materials Science and Engineering, Shanghai University, 333 Nanchen Road, Shanghai 200444, China. E-mail: runxu@shu.edu.cn*
[b]*Zhejiang Institute of Advanced Materials, SHU, 1588 Huaxiang Street, Jiashan 314113, China*
[c]*Department of Physics, College of Sciences, Shanghai University, 99 Shangda Road, Shanghai 200444, China*
[d]*Shanghai Technical Institute of Electronics & Information, 3098 Wahong Road, Shanghai 201411, China*
[e]*Hebei Institute of Pure Iron Materials and Application Industry Technology, Handan 056300, China*
†Electronic supplementary information (ESI) available: Solubilities in different solvents, Tyndall effect, crystal structure, XRF, XPS, PL intensity and FWHM, and electronic performance. See DOI: https://doi.org/10.1039/d3qi02153j

Introduction

Compared to polycrystalline films, nanocrystals, and nanowires, high-quality metal halide perovskite (PVK) single crystals with lower trap density may be considered to be the most attractive emerging materials for detection applications.[1] Solution growth has become a mainstream method for the growth of PVK single crystals due to the low cost of the equipment, the simplicity of operation and the ease of growth into crystals with good homogeneity and complete shape.[2,3] The choice of solvent, solubility and temperature are critical factors affecting the growth rate and quality of single crystals, with solubility being particularly crucial. Excessive solute solubility makes it challenging to precipitate crystals from the solution, while low solubility restricts the size and growth rate of the crystals. Ideally, the growing material should have moderate solubility in the solvent, with a sufficient solubility gradient. Compared to organic–inorganic hybrid PVKs, all-inorganic perovskites are more stable and less prone to decomposition, thus making it difficult for them to grow into large sized crystals in solution due to the relatively low solubility.[4] In particular, chlorine-based inorganic perovskites have a larger bandgap than iodine- and bromine-based inorganic PVK, making them more suitable for visible-blind ultraviolet[5,6] (UV) detector applications. Fang *et al.* have demonstrated that it is difficult to fabricate high-quality wide bandgap $CsPbCl_3$ because of the poor solubility of $CsCl$ and $PbCl_2$ in dimethylsulfoxide (DMSO).[7] Actually, the UV detectors prepared by chlorine-based inorganic perovskite single crystals have been rarely reported due to their low solubilities, which limit the quality and size of solution-grown single crystals and seriously

This journal is © the Partner Organisations 2024

Inorg. Chem. Front., 2024, **11**, 589–601 | **589**

hinder their commercial applications. Therefore, understanding the reasons for the low solubility of chlorine-based inorganic perovskites and exploring effective ways to increase their solubility are critical priorities for improving single crystal growth. In this work, we chose the environmentally friendly $Cs_mSb_nCl_{m+3n}$ (CSC) perovskite as a typical material to investigate the dissolution conditions in single crystal growth, as it has the lowest solubility among the reported chlorine-based inorganic PVKs.

$Cs_mSb_nCl_{m+3n}$ is a low-dimensional perovskite structure material derived from the traditional three-dimensional (3D) ABX_3 (A = $CH_3NH_3^+$, $CH(NH_2)_2^+$, Cs^+; B = Pb^{2+}, Sn^{2+}; X = I^-, Br^-, Cl^-) perovskite, which overcomes the issues of phase transformation and instability of 3D PVKs.[8] Sb-based PVKs have the same lone-pair ns^2 outermost electronic configuration of the Sb^{3+} element as for Pb^{2+}, resulting in similar photoelectric properties to those of Pb-based PVK materials.[9] The history of the synthesis of trigonal and orthorhombic $Cs_3Sb_2Cl_9$ could be backtracked to 1970,[10] while most reports have focused on the preparation of nanowires,[11] nanocrystals,[12] and thin films.[13] Pradhan and co-workers synthesized $Cs_3Sb_2Cl_9$ PVK nanowires with lengths up to several microns by a colloidal route and fabricated a $Cs_3Sb_2Cl_9$ nanowire-based photodetector with a detectivity of 1.25×10^6 Jones, as well as the rise time and decay time of 0.13 s and 0.23 s, respectively.[11] There are still no relevant reports on the growth of centimeter-sized $Cs_3Sb_2Cl_9$ single crystals and the fabrication of the corresponding UV detector. As mentioned above, the main challenge comes from the fact that the raw materials of CSC (CsCl and $SbCl_3$) are difficult to dissolve in a conventional single solvent simultaneously, and the solubility of the precursor solution is too low to grow CSC single crystals.[13] The solution-based growth of single crystals depends strongly on the precursor solvent, which can be divided into aqueous acid solvents (*e.g.*, hydroiodic acid, hydrobromic acid, and hydrochloric acid) and organic solvents (*e.g.*, *N,N*-dimethylformamide (DMF), γ-butyrolactone (GBL), DMSO, *N*-methyl pyrrolidone (NMP), acetone, ethanol, isopropanol, *etc.*). Unfortunately, neither of the aforementioned solvent types can dissolve the $Cs_3Sb_2Cl_9$ precursor at high concentrations. Among only a few reports, $Cs_3Sb_2Cl_9$ is obtained by cooling or evaporating a mixed solution of CsCl and $SbCl_3$[10,14] or Sb_2O_3[15,16] dissolved in dilute hydrochloric acid, while the solubility is still insufficient to grow large-sized $Cs_3Sb_2Cl_9$ single crystals. Therefore, it is imperative to improve the solubility of the precursor solution and grow high-quality centimeter-sized $Cs_3Sb_2Cl_9$ single crystals for application in ultraviolet photodetectors.

In this work, we have successfully prepared clear PVK precursor solutions using hybrid solvents with enhanced solubility due to the presence of both $SbCl_x^{3-x}$ colloids and Cs^+ ions in the solution. By controlling the molar ratio of the raw materials, the centimeter-sized all-inorganic α-$Cs_3Sb_2Cl_9$ and $Cs_5Sb_2Cl_{11}$ perovskite single crystals were grown through the gradient cooling temperature crystallization method (GCTCM). The structural characterization and optical properties of the

prepared CSC single crystals have been systematically investigated, confirming that CSC is an ideal material for photodetectors sensing UV light radiation. The visible-blind ultraviolet photodetectors based on CSC single crystals were fabricated, demonstrating good wavelength selectivity and fast response speed.

Experimental

Materials and chemicals

Cesium chloride (CsCl, 99.9%, Xi'an Polymer Light Technology Corp), Antimony(III) chloride ($SbCl_3$, 99.99%, Aladdin), dimethylsulfoxide (DMSO, 99.9%, Aladdin), ethyl alcohol (GR, Sinopharm), isopropanol (AR, Sinopharm), *N*-methyl pyrrolidone (NMP, 99.9%, Aladdin), *N,N*-dimethylformamide (DMF, 99.9%, Aladdin), γ-butyrolactone (GBL, 99%, TCI), hydrochloric acid (HCl, 37 wt%, Sinopharm).

Perovskite precursor solution preparation

It was obvious that the inherent concentration of dilute hydrochloric acid and the volume ratio of hydrochloric acid to DMSO directly affect the concentration of the precursor solution, therefore, their effects on the solubility were investigated. The solubility of the mixed powders of CsCl and $SbCl_3$ exhibited an increasing-then-decreasing trend as the inherent concentration of hydrochloric acid decreased, while maintaining the fixed volume ratio of DMSO to dilute hydrochloric acid (4 : 1). It reached its maximum value at a concentration of 8 wt%, as shown in Fig. S1 in the ESI.† Subsequently, the inherent concentration of hydrochloric acid in the hybrid solvent was set to 8 wt%, and the optimal solubility of CsCl and $SbCl_3$ mixed powders was attained at a DMSO to HCl volume ratio of 3 : 1. This ratio was found to be the most effective after considering alternative ratios of 2 : 1, 3 : 1, 4 : 1, and 1 : 4.

As a result, the DMSO : HCl (8 wt%) mixture with a volume ratio of 3 : 1 was finally selected as the hybrid solvent for the preparation of the precursor solution. Then CsCl and $SbCl_3$ are dissolved in the as prepared 3DMSO : HCl (8 wt%) solvent mixture with molar ratios of 3 : 2 and 5 : 2, respectively. The mixture solution was stirred at 90 °C overnight.

Single crystal growth

CSC single crystals were prepared *via* the controlled gradient cooling temperature crystallization method. The as-prepared perovskite precursor solution was maintained at 95 °C, then the temperature was decreased by 5 °C every 6 hours to 80 °C, and then lowered by 4 °C every 12 hours to 60 °C, and subsequently cooled at a rate of 2 °C day^{-1} until 54 °C, at which stage single crystals began to appear, and then continuously cooled at a rate of 2 °C day^{-1} to allow the single crystals to slowly grow. Centimeter-sized single crystals of pale-yellow color α-$Cs_3Sb_2Cl_9$ and colorless $Cs_5Sb_2Cl_{11}$ were obtained after 14 days.

590 | *Inorg. Chem. Front.*, 2024, **11**, 589–601

This journal is © the Partner Organisations 2024

Characterization

Powder XRD patterns were recorded using an X'Pert[3] powder X-ray diffractometer (Malvern Panalytical) equipped with a Cu tube operated at 40 kV and 30 mA. The X-ray intensity data of CSC single crystals were measured on a Bruker D8 VENTURE DUO PHOTON III Bruker APEX-II CCD system equipped with an Incoatec Ius 3.0 Microfocus sealed tube (Mo Kα, λ = 0.71073 Å) and a Helios MX Multilayer Optical monochromator. The Rietveld refinements were performed by using a Bruker SHELXTL software package. The high-resolution X-ray rocking curve (XRC) was obtained using an Empyrean multifunctional X-ray diffractometer (Malvern Panalytical), with a Cu Kα1 line operated at V = 40 kV and I = 20 mA. The Raman spectroscopy studies were performed by using a Horiba Jobin Yvon LabRAM HR800 Raman spectrometer with an ultraviolet pulsed 355 nm laser beam as the excitation source. XRF spectra were measured with MXF-2400 multi-channel X-ray fluorescence spectrometer (Shimadzu). XPS spectra were measured using an Escalab 250Xi photoelectron spectrometer (Thermo Scientific). The UV-Vis absorbance and transmittance spectra were recorded at room temperature using a PerkinElmer Lambda 950 UV–vis–NIR spectrophotometer with a scan speed 300 nm min^{-1} and a slit width quantitative 5 nm in a wavelength range of 200–900 nm at room temperature. A highly refined barium sulfate ($BaSO_4$) plate was used as the reference (100% reflectance). The temperature-dependent steady-state photoluminescence (PL) spectra were recorded on an RF-5301pc spectrofluorometer (Shimadzu) with the operating temperature ranging from 10 K to 275 K using the 266 nm laser beam. Time-resolved emission data were collected at room temperature using a FluoroMax spectrofluorometer (Horiba). The dynamics of emission decay was monitored by using a FluoroMax spectrofluorometer with time-correlated single-photon counting capability (4096 channels) with data collection for 10 000 counts.

Theoretical calculations

Defect calculations were performed in the framework of DFT using the projector-augmented wave (PAW) method, and the screened hybrid Heyd–Scuseria–Ernzerhof (HSE) functionals, as implemented in the Vienna *Ab initio* simulation package (VASP).[17] The plane-wave cutoff energy was set to 450.0 eV. The van der Waals (vdWs) dispersion correction was applied and described by the DFT-D3 correction.[18] The employed primitive cell and Γ-centered k-mesh are $7 \times 7 \times 5$ for α-$Cs_3Sb_2Cl_9$ and $4 \times 4 \times 4$ for $Cs_5Sb_2Cl_{11}$, respectively. The lattice parameters and atomic positions of all the structures were relaxed until the Hellmann–Feynman forces on them were smaller than 0.01 eV Å^{-1}. The calculated lattice constants are $a = b = 7.7966$ Å, $c = 9.5322$ Å for α-$Cs_3Sb_2Cl_9$, and $a = 13.6997$ Å, $b = 12.8955$ Å, and $c = 14.7419$ Å for $Cs_5Sb_2Cl_{11}$, respectively.

Device fabrication and detection performance characterization

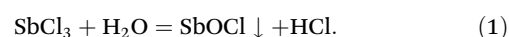To prepare CSC photodetectors, these polished single crystals were sandwiched between the rectangular electrodes (2 mm × 2 mm) Au (50 nm), and then deposited on both sides of the single crystal using a thermal evaporator. The current–voltage (I–V) curves of photodetectors in the dark and under different irradiation were measured (2400 Series source meter, Keithley Instruments Inc.) by using a 266 nm laser beam with the bias voltage in the range from −30 V to 30 V. The time-dependent photoresponse signal was recorded using a 1 GHz digital oscilloscope with a Keithley 428 current amplifier. The spectral responsivity was measured using a monochromator combined with an optical chopper and a lock-in amplifier. The light intensity was calibrated by a UV enhanced silicon photodetector in the wavelength range of 200–700 nm. All the optoelectronic properties were measured under the atmospheric environment.

Results and discussion

Solvent for the preparation of the precursor solution

In the process of growing single crystals by the solution method, the preparation of the precursor solution is of crucial importance. According to the "like dissolves like" rule, solutes composed of polar molecules are easily soluble in polar solvents and difficult to dissolve in nonpolar solvents. Therefore, polar solvents should be employed to dissolve $SbCl_3$, while CsCl, an ionic crystal, can be ionized in polar solvents to produce charged anions and cations. Since solvent molecules in polar solvents have positive and negative polarity, there is a strong attraction between solvent molecules and solute ions. This attraction allows the anions and cations to overcome the Coulomb attraction between each other and diffuse into the solvent. Therefore, CsCl can be dissolved in solvents with large polarity. In order to obtain stable precursor solutions with high concentrations, a variety of polar solvents are used in the experiment for the dissolution of the CsCl, $SbCl_3$, CsCl and $SbCl_3$ mixture with a mole ratio of 3 : 2, and $Cs_3Sb_2Cl_9$ powder synthesized as reported, including DMSO, DMF, NMP, GBL, hydrochloric acid, ethanol, isopropanol, and deionized water, *etc*. As listed in Table S1 in the ESI,† CsCl is highly soluble in deionized water and hydrochloric acid, but hardly dissolves in organic solvents due to the different polarities of these solvents. The order of polarity of the solvents is as follows, water > DMSO > NMP > DMF > ethanol > isopropanol > GBL, the solubility of CsCl decreases with the decrease of solvent polarity. Also note that $SbCl_3$ with more covalent bonds is easily soluble in both organic solvents and hydrochloric acid at high concentrations, while it is difficult to dissolve in deionized water and undergoes a hydrolysis reaction as indicated by the following eqn (1),

$$SbCl_3 + H_2O = SbOCl \downarrow + HCl. \tag{1}$$

Since either CsCl or $SbCl_3$ is easily soluble in hydrochloric acid, it could be supposed that the mixture of CsCl and $SbCl_3$ can dissolve well in this solution. Unfortunately, the mixture of CsCl and $SbCl_3$, as well as $Cs_3Sb_2Cl_9$ powder, are all much more difficult to dissolve in hydrochloric acid, and organic sol-
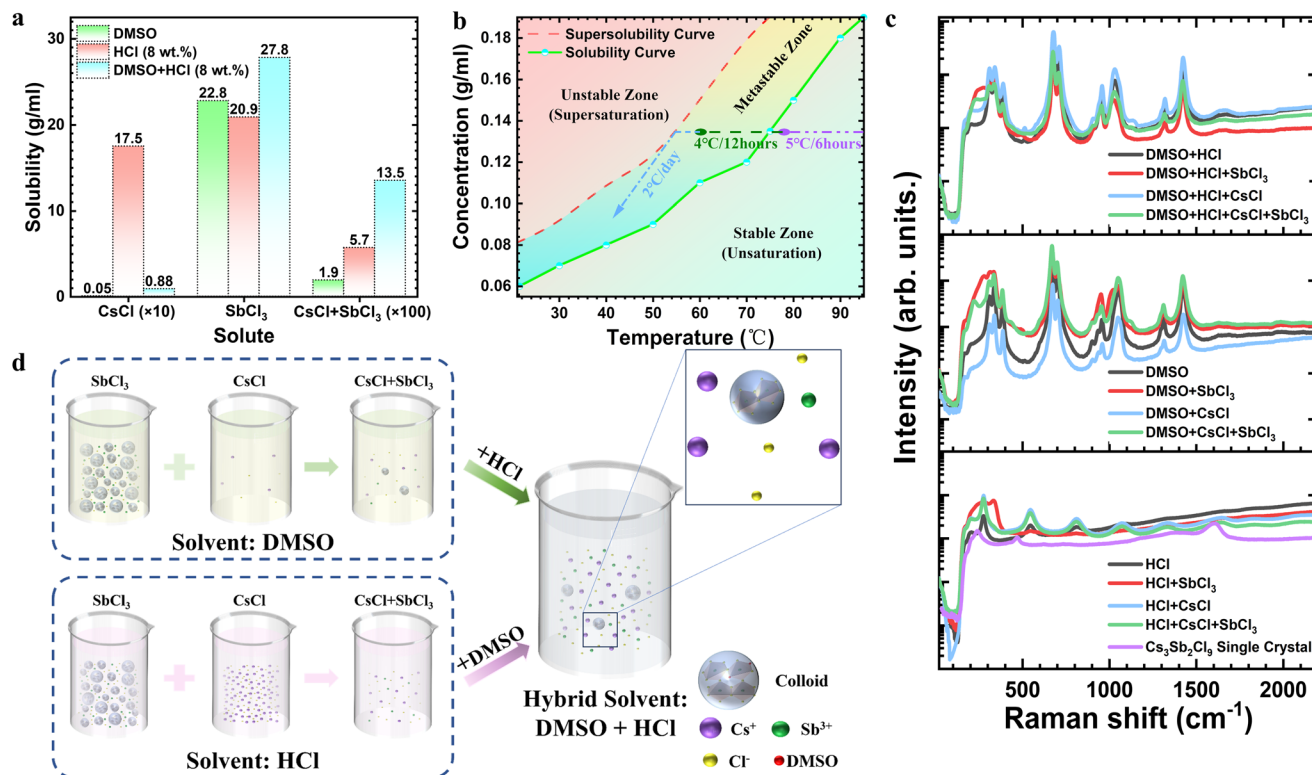
vents as well (Table S1† and Fig. 1a). It is noteworthy that the solubility of CsCl and SbCl$_3$ mixed powders in DMSO is the lowest, only 0.019 g ml^{-1}, which can give rise to the difficulty of dissolving CsCl in DMSO (0.005 g ml^{-1}). Therefore, the low solubility of the Cs$_3$Sb$_2$Cl$_9$ precursor solution by using a single solvent makes the growth of a large single crystal almost impossible.

Then, several hybrid solvents were investigated, and it was found that the hybrid solvent mixed with DMSO and hydrochloric acid can improve the solubility of Cs$_3$Sb$_2$Cl$_9$, as shown in Fig. 1a, b, and Fig. S1.† The solubility of the mixed powders in the hybrid solvent of DMSO and hydrochloric acid (8 wt%) is 0.135 g ml^{-1}, which is more than 6 times higher than that in DMSO and almost 2.5 times as high as that in hydrochloric acid (8 wt%).

In order to reveal the reason for the increase in solubility in the hybrid solvent, the existing modes of solutes in each solvent were investigated. As shown in Fig. S2,† the typical Tyndall effect was observed for SbCl$_3$ in all three solvents, indicating that SbCl$_3$ could be coordinated in the solvent[19] and form various coordination products of SbCl$_x^{3-x}$, such as SbCl^{2+}, SbCl$_2^+$, SbCl$_3$, SbCl$_4^-$, SbCl$_5^{2-}$, and SbCl$_6^{3-}$, similar to that reported for PbI$_2$.[20] In contrast, after the addition of CsCl, the intensity of the Tyndall effect has become lower, indicating

that the addition of CsCl disrupts part of the SbCl$_x^{3-x}$ framework and reduces the number of colloids, especially in hydrochloric acid, where the Tyndall effect is no longer observed, suggesting that colloids are completely decomposed by the combined action of H$^+$ and Cs$^+$,[21,22] and the solute exists in the ionic state in hydrochloric acid.

In addition, the Raman spectra of the prepared well-stirred solutions can confirm the above results about the type of solute particles present in solutions. As shown in Fig. 1c, the Raman peak positions of CsCl in solution basically overlap with those of the pure solvent, regardless of whether it is dissolved in a single solvent or a hybrid solvent, since CsCl is an ionic crystal that presents in the solvent as Cs$^+$ and Cl$^-$ ions. In contrast, the Raman spectra of SbCl$_3$ in all solutions show a noticeable peak shape variation at the region of 230, 276, and 339 cm^{-1} shift, which should be assigned to the Sb–Cl stretching vibrational bands.[23,24] It is worth noting that the peak position and shape of the Raman spectra of the CsCl and SbCl$_3$ mixed powders in DMSO and DMSO : HCl (8 wt%) are consistent with that of SbCl$_3$ in the corresponding solvent under the same SbCl$_3$ mole concentration, with only a slight decrease in the intensity of the Sb–Cl peak, confirming that the addition of CsCl causes the partial decomposition of the SbCl$_x^{3-x}$ colloids and a decrease in the number of colloids. In

Fig. 1 Dissolution conditions in different solvents. (a) Solubilities of CsCl, SbCl$_3$, CsCl and SbCl$_3$ mixed powders in different solvents at 75 °C. For a clearer presentation, the solubility values of CsCl are multiplied by 10, and that of CsCl + SbCl$_3$ mixed powders are multiplied by 100. (b) Solubility curve and concentration at different temperatures. (c) Raman spectra of the upper clear layers of the well-stirred solutions prepared by CsCl, SbCl$_3$, and CsCl and SbCl$_3$ mixed powders. Black: pure solvent, red: SbCl$_3$ solution, blue: CsCl solution, green: solution prepared using CsCl and SbCl$_3$ mixed powders. (d) Schematic diagram of the precursor solution state.

comparison, the peak positions of the CsCl and $SbCl_3$ mixed powders in hydrochloric acid basically overlap with that of the hydrochloric acid itself, but are very different from that of $SbCl_3$ dissolved in hydrochloric acid, with no characteristic Sb–Cl peak, indicating the absence of colloids, which is consistent with the results of the Tyndall effect.

A schematic diagram shown in Fig. 1d can then demonstrate the evolution of the type of solute particles present in precursor solutions from a single solvent to a hybrid solvent, as evidenced by the Raman spectra and the Tydnall effect described above. As shown in Fig. 1c, the solubility of either CsCl or $SbCl_3$ powders alone is high in hydrochloric acid (8 wt%), while the solubility decreases substantially once these two powders are mixed. This is because the addition of Cs^+ into $SbCl_3$ solution can decompose a large number of $SbCl_x^{3-x}$ frameworks into ions, so that the ion concentration reaches supersaturation, thus forming CSC precipitates. When DMSO is added to the hydrochloric acid precursor, a small amount of $SbCl_x^{3-x}$ colloids could exist stably in the hybrid solvent, leading to the improvement of solubility. This result is consistent with the report by Snaith et al.,[21] from which it can also be deduced that the presence of colloids can lead to the improvement of the solute solubility. On the other hand, CsCl is almost completely insoluble in DMSO, while the addition of hydrochloric acid into DMSO can raise the solubility of CsCl substantially (0.088 g ml^{-1}), thus greatly improving the solubility of the mixed powders in the hybrid solvent of DMSO and hydrochloric acid. These results strongly suggest that the hybrid solvent of DMSO and hydrochloric acid is more suitable as the precursor solution to grow large-sized CSC single crystals.

The saturated solubility curve of CSC in this hybrid solvent measured at different temperatures is shown in Fig. 1b, which increases with the increase of temperature, showing the positive temperature crystallization characteristics of CSC. The solubility curve and the super-solubility curve divide the diagram into three regions, i.e., the unsaturated, supersaturated, and metastable regions. It is the metastable region that is much more suitable for large crystal growth, in agreement with $CH_3NH_3PbI_3$.[25] In this study, pale-yellow color single crystals with the size of $10 \times 8 \times 2$ mm^3 and colorless single crystals with the size of $11 \times 9 \times 4$ mm^3 were prepared via the controlled gradient cooling temperature crystallization method using the CsCl and $SbCl_3$ mixture in stoichiometric ratios of $3:2$ and $5:2$, respectively, for details see the Materials and methods section. Different cooling rates are used to step down the temperature at different stages of crystal growth. At the initial stage, the temperature was lowered at a fast rate (5 °C every 6 hours) to near the solubility curve, then at a slow rate (4 °C every 12 hours) in the metastable region to near the super-solubility curve, and finally at a very low rate (2 °C day^{-1}) before and after the precipitation of the seed crystals, so that the crystals were grown slowly in the metastable region to grow large single crystals.
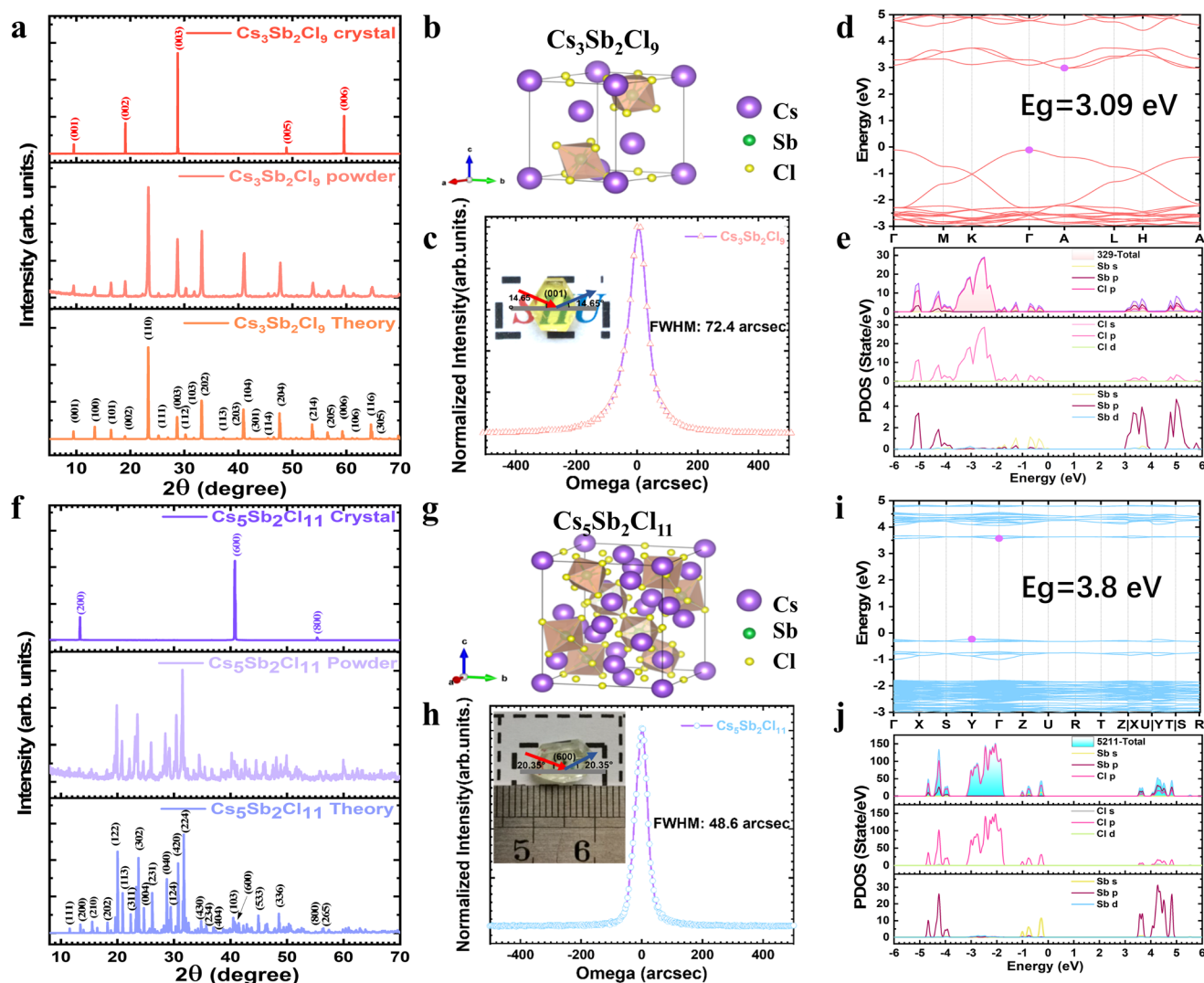
Structural characterization of $Cs_3Sb_2Cl_9$ and $Cs_5Sb_2Cl_{11}$

These as-grown single crystals were characterized using single-crystal X-ray diffraction (SCXRD) and double-axis high-resolution X-ray rocking curve (XRC) for the study of the structure, while powders milled from the crystals were characterized by powder X-ray diffraction (PXRD) technology. The PXRD results shown in Fig. 2a demonstrate that the as-obtained pale-yellow color single crystals are in perfect agreement with the theoretical data of α-$Cs_3Sb_2Cl_9$, which possesses a crystal structure with the trigonal space group of $P321$. The θ–2θ X-ray measurement for the surface growth plane of the crystal shows only five sharp and narrow diffraction peaks along the (001) plane, indicating the good crystallinity of α-$Cs_3Sb_2Cl_9$ single crystals. As shown in Fig. 2b and Fig. S3,† the crystal structure of the 2D layered α-$Cs_3Sb_2Cl_9$ is derived from the hypothetical perovskite compound $CsSbCl_3$ (i.e., $Cs_3Sb_3Cl_9$) by removing every third Sb layer along $\langle 111 \rangle$ to achieve correct charge balance.[26,27] The trigonal unit cell is built of isolated layers formed by six-membered rings of $SbCl_6$ octahedra pointed up and down alternatively with respect to the plane of common atoms Cl, and the monovalent cesium cations are located in the large cavities formed in the center of those rings and below or above each $SbCl_6$ octahedra thus filling all empty folds within the layer.[28] The unit cell parameters, $a = b = 7.809$ Å, $c = 9.574$ Å, $\alpha = \beta = 90°$, $\gamma = 120°$, are presented in Table S2 in the ESI.† As a result of distortion, two different bond lengths for the Sb–Cl bonds are observed in the $SbCl_6$ octahedron, which for Sb–Cl1 and Sb–Cl2 are calculated to be 2.847 Å and 2.528 Å, respectively.

The structure of the colorless single crystal was solved and refined using the Bruker SHELXTL Software Package, the SCXRD data are shown in Fig. 2f, fitting the space group $Pbca$, with $Z = 4$ for the formula unit, $Cs_5Sb_2Cl_{11}$, which are also consistent with the PXRD measurements. The X-ray 2θ scan on the growth plane of $Cs_5Sb_2Cl_{11}$ (CCDC 2307326) shows only (200), (600), and (800) diffraction peaks, suggesting good single crystalline quality, as do the grown α-$Cs_3Sb_2Cl_9$ crystals. The XRD studies reveal that $Cs_5Sb_2Cl_{11}$ crystallizes at room temperature in orthorhombic symmetry with the following lattice constants: $a = 13.1584$ (3) Å, $b = 12.4187$ (4) Å, $c = 14.4150$ (4) Å, volume $= 2355.56$ (11) Å^3, as shown in Fig. 2g and Tables S3–S5 in the ESI.† The $Cs_5Sb_2Cl_{11}$ crystal is built up of cesium cations and discrete $[Sb_2Cl_{11}]^{5-}$ groups, which represent a new type of halide complex, such as $(CH_3NH_3)_5Bi_2X_{11}$ type crystals.[29–31] $[Sb_2Cl_{11}]^{5-}$ consists of two $SbCl_6$ octahedra joined via one chlorine bridge, in which the bridging Sb–Cl (1) bond is longer (2.8920 Å) and the Sb–Cl (4) bond along the direction of the Sb–Cl (1) bond is shorter (2.4592 Å) than the other four terminal bonds (between 2.5629 and 2.7057 Å), and most of these bond angles are about 90 or 180°.[32]

The phase purity and crystallinity of the as-grown crystals were confirmed by XRD scans of the growth plane and corresponding power, and the crystalline quality was evaluated by XRC. We performed the XRC of (003) diffraction for as-grown $Cs_3Sb_2Cl_9$ crystals and (600) diffraction for $Cs_5Sb_2Cl_{11}$ crystals, respectively, as illustrated in Fig. 2c and h. The full width at half maximum (FWHM) of the XRC peak was found to be 72.4 arcsec for as-grown $Cs_3Sb_2Cl_9$ crystals, and 48.6 arcsec for $Cs_5Sb_2Cl_{11}$ crystals, demonstrating good crystalline quality comparable to conventional Pb-based halide PVK crystals.[25,33]

This journal is © the Partner Organisations 2024

Inorg. Chem. Front., 2024, 11, 589–601 | 593

Fig. 2 Structural Characterization of $Cs_3Sb_2Cl_9$ and $Cs_5Sb_2Cl_{11}$. (a) and (f) X-ray diffraction curve of calculated data, ground powder from large CSC single crystals, and as-grown single crystals. (b) and (g) Crystal structure of the CSC unit cell. (c) and (h) X-ray rocking curves of CSC single crystals. Insets: photographs of the as-grown crystals. (d) and (i) The electronic band structures of CSC and the band edge positions are indicated by the red and blue dots, highlighting the nature of indirect band gaps in these materials. (e) and (j) Electronic DOS for CSC crystals. (a)–(e) $Cs_3Sb_2Cl_9$. (f)–(j) $Cs_5Sb_2Cl_{11}$.

To explore the elemental compositions of the crystals, they were measured by X-ray fluorescence (XRF) techniques. As shown in Fig. S4,† the XRF data show an atomic ratio of Cs/Sb/Cl $\approx 2.9 : 2 : 8.9$, which matches closely to the $Cs_3Sb_2Cl_9$ chemical composition. As for the XRF data of as-grown $Cs_5Sb_2Cl_{11}$ crystals, the atomic ratio of Cs/Sb/Cl is about $5 : 2.1 : 12.7$, close to the stoichiometric ratio of $Cs_5Sb_2Cl_{11}$, but there is a slight excess of $SbCl_3$ on the crystal surface. Further evidence of component analysis shows the characteristic peaks for Cs, Sb, and Cl *via* X-ray photoelectron spectroscopy (XPS) measurements (Fig. S5†). XPS spectra confirm the presence of Cs^+, Sb^{3+} and Cl^- states within the CSC crystals, for example, the Sb $3d_{3/2}$ and $3d_{5/2}$ doublet peak with binding energies of 539.7 and 530.5 eV are corresponding to the Sb^{3+} state.[34] Note that the calculated atomic ratio of Cs/Sb/Cl for the $Cs_5Sb_2Cl_{11}$

crystal is around $5 : 2.9 : 12.5$, which is similar to the result of XRF. Excess $SbCl_3$ may be resulting from the etching process[35] during the removal of the crystals from the growth solution, and the same phenomenon was found for $CH_3NH_3PbI_3$.

Since the band gap is the key quantity for selecting photo-detector materials, it is hence calculated using the Heyd–Scuseria–Ernzerhof (HSE) hybrid functional,[36–38] with full details provided in the Experimental section, as the hybrid density functional usually gives the accurate fundamental band gaps for most semiconductors. As illustrated in Fig. 2d and i, band edge positions in band structures are indicated by the red and blue dots, highlighting the nature of indirect band gaps of CSC materials. The indirect bandgap of $Cs_3Sb_2Cl_9$ is 3.09 eV, while that of $Cs_5Sb_2Cl_{11}$ is 3.80 eV, both of which are well suited for UV detectors. The projected density of states

(PDOS) for CSC are shown in Fig. 2e and j. The semi core state of Cs p states forms a narrow band located at a deep energy of −8 eV, and have almost no contribution to the valence band maximum (VBM) and conduction band minimum (CBM), the same as other CsBX$_3$ PVKs.[36] With regard to Cs$_3$Sb$_2$Cl$_9$, there is a couple of Sb s peaks located at positions ranging from −2 to 0 eV, which overlap the Cl p state, indicating a hybrid state of Sb s and Cl p states. The valence band edge (−2 to 0 eV) of Cs$_3$Sb$_2$Cl$_9$ is dominated by the Cl p and Sb s hybrid state, while the contribution of Sb p to the VBM is also identifiable but fairly small. The conduction band edge is predominantly derived from a hybrid state of Sb p and Cl p states, which can be observed in the energy range between 3 and 6 eV. When it comes to Cs$_5$Sb$_2$Cl$_{11}$, a hybrid state of Sb s and Cl p states is observed in the energy range from −1.3 to 0 eV, dominating the valence band edge, whereas the Sb p and Cl p hybrid state contributes to the conduction band edge, which localizes in the energy range between 3.3 and 5 eV. As reported by Saparov and his co-workers, smaller lattice constants indicate stronger cation–anion bonding, resulting in more dispersive bands.[27] The calculated band structure shown in Fig. 2d reveals a dispersive character for the upper valence band of the 2D Cs$_3$Sb$_2$Cl$_9$ perovskite, which can be understood by the strong Cl p–Sb s antibonding coupling,[39] similar to the case of 3D CH$_3$NH$_3$PbI$_3$. Whereas Cs$_5$Sb$_2$Cl$_{11}$ has flatter valence bands (Fig. 2i) than 2D Cs$_3$Sb$_2$Cl$_9$, due to its zero-dimensional structural characteristic, which is consistent with other 0D materials.[39,40]

Optical properties of Cs$_3$Sb$_2$Cl$_9$ and Cs$_5$Sb$_2$Cl$_{11}$

The optical absorbance and transmittance of as-grown single crystals were further investigated by UV–vis spectroscopy as shown in Fig. 3a. The transmittances of Cs$_5$Sb$_2$Cl$_{11}$ and Cs$_3$Sb$_2$Cl$_9$ can approach 93% and 87% at 600 nm, respectively, both higher than those of the typical lead-free PVK single crystals reported.[41–44] It should be noted that both the absorption and transmittance spectra of Cs$_5$Sb$_2$Cl$_{11}$ exhibit a noticeable blue shift compared with those of Cs$_3$Sb$_2$Cl$_9$. Such a blue shift in the absorption and transmittance spectra is consistent with the blue shift observed in the photoluminescence (PL) spectra, confirming that the absorption edge shift results from a larger bandgap of Cs$_5$Sb$_2$Cl$_{11}$. The optical bandgaps of the CSC crystals are fitted by Tauc[45] eqn (2),

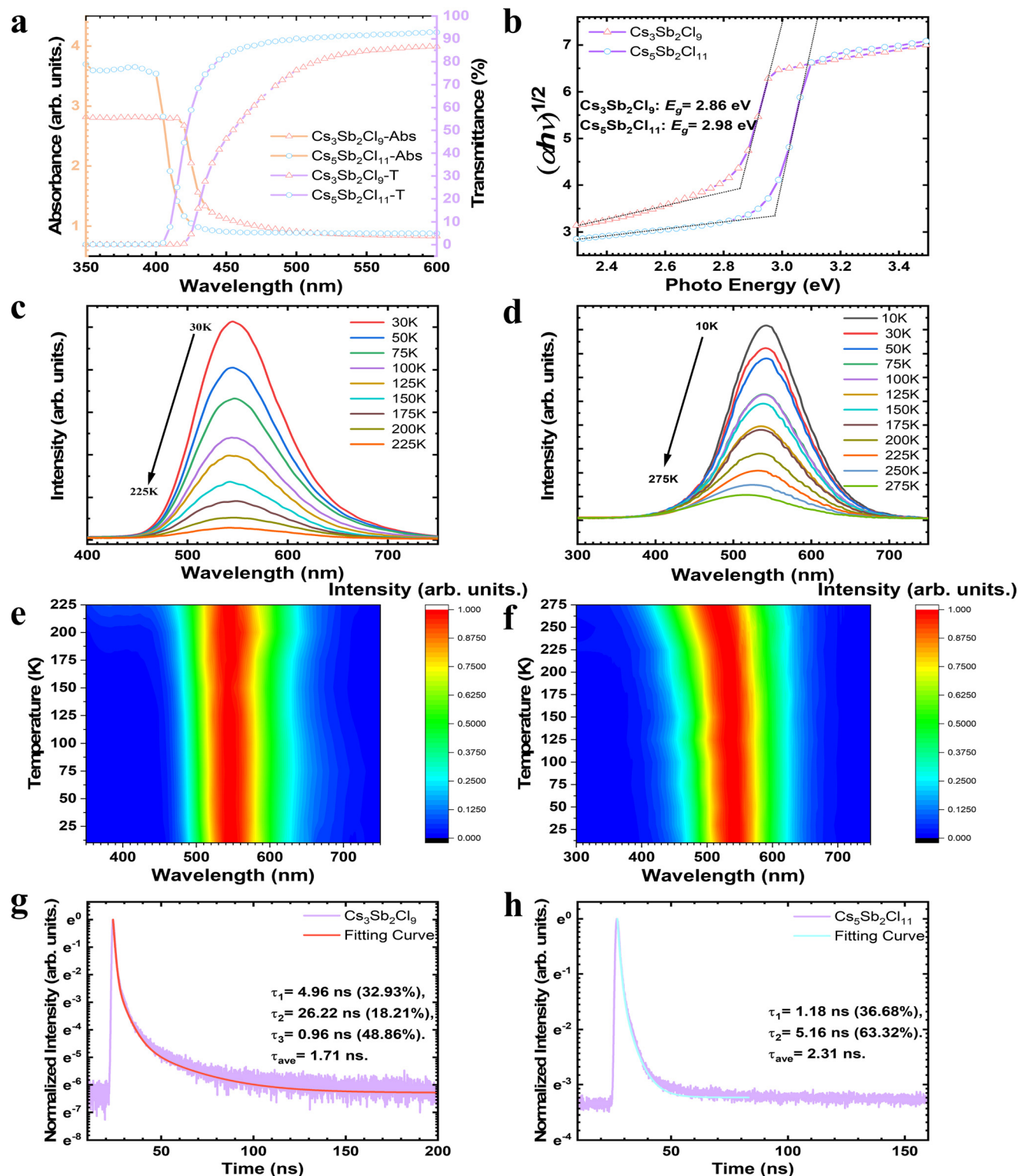$$(\alpha h\nu)^{1/2} = A(h\nu - E_g) \tag{2}$$

where α is the absorption coefficient, $h\nu$ is the photon energy, A is the constant, and E_g is the optical bandgap. The optical band gaps of as-grown CSC crystals were calculated to be 2.86 eV for Cs$_3$Sb$_2$Cl$_9$ and 2.98 eV for Cs$_5$Sb$_2$Cl$_{11}$, respectively (Fig. 3b). This result provides further evidence of the suitability of CSC crystals for UV detection. It is worth mentioning that the optical band gaps of both CSC materials are smaller than the calculated values by HSE. The bandgap mismatch between the experimental and calculated values of Cs$_3$Sb$_2$Cl$_9$ is small, while that of Cs$_5$Sb$_2$Cl$_{11}$ is large.

Temperature-dependent photoluminescence spectra excited using a 266 nm laser beam were recorded to investigate the properties of exciton and electron–phonon interactions. The broad emission spectrum (from 450 to 750 nm for Cs$_3$Sb$_2$Cl$_9$, from 400 to 700 nm for Cs$_5$Sb$_2$Cl$_{11}$) suggests that near edge defects levels related to surface states or vacancies take part in the emission process. The emission peak is located at 542 nm for Cs$_3$Sb$_2$Cl$_9$ and 532 nm for Cs$_5$Sb$_2$Cl$_{11}$ at 225 K, respectively (Fig. 3c and d). All CSC crystals exhibit a similar behavior that the integrated PL intensity decreases while the FWHM increases with the operating temperature (Fig. 3e, f and Fig. S6†), and the PL peak position exhibits a small blueshift, which is attributed to the effects of electron–phonon interactions. Decreasing temperature leads to a decrease in thermal ionization energy, enabling more excitons to compound and resulting in a gradual increase in luminescence at low temperatures. This suggests that the luminescence is associated with self-trapped excitons (STEs) originating from excited-state structural distortions of the SbCl$_6$ octahedra at room temperature.[40,46,47]

Furthermore, the normalized time resolved PL (TRPL) decay plots were measured under ambient conditions at an excitation wavelength of 380 nm and the decay traces were fitted using multiexponential decay kinetics as reported (Fig. 3g and h). For the Cs$_3$Sb$_2$Cl$_9$ crystal, the decay time extracted from the fitting curve showed an initially fast component with a lifetime of 0.96 ns, followed by two slow components with lifetimes of 4.96 ns and 26.22 ns, while for the Cs$_5$Sb$_2$Cl$_{11}$ crystal, a fast component with a lifetime of 1.18 ns and a slow component with a lifetime of 5.16 ns were obtained. In general, the fast component is regarded as originating from the high trap density related to the crystal surface, and the slow component represents the carrier transportation in the bulk crystal with fewer traps.[48,49] All CSC crystals exhibit PL decay times on the nanosecond scale with the value of 1.71 ns for Cs$_3$Sb$_2$Cl$_9$ and 2.31 ns for Cs$_5$Sb$_2$Cl$_{11}$, respectively, which are in good agreement with the ones reported recently for the Pb-free PVK single crystals.[43,50,51]
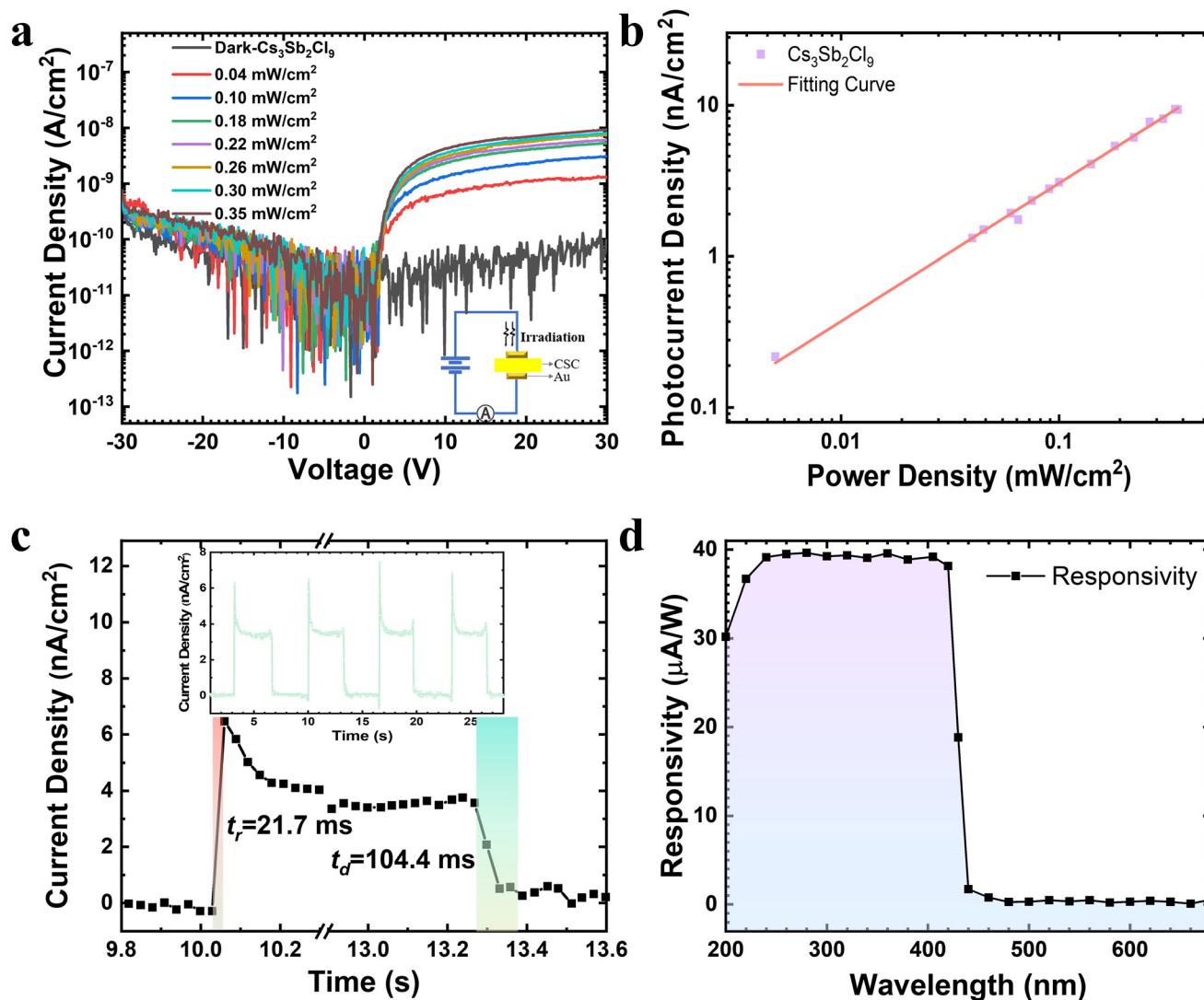
Device performances of CSC single-crystal photodetectors

To characterize the electrical properties of CSC single-crystal detectors, two 50 nm Au electrodes with 2 × 2 mm^2 were deposited on the surface of polished 2 mm thick CSC single crystals to fabricate photodetectors based on the Au/CSC/Au structure, as shown in the inset of Fig. 4a. It is common knowledge that dark current and photocurrent are important parameters to characterize the performance of semiconductor photodetectors, and are the representations of the carrier transport capacity. In Fig. 4a and Fig. S7,† the typical current–voltage curves of the prepared CSC single-crystal photodetectors clearly show its nonlinear behaviors, indicating the formation of a back-to-back Schottky contact.[52] Moreover, the Cs$_3$Sb$_2$Cl$_9$ single crystal shows a very low dark current density of around 9.08 × 10^{-11} A cm^{-2} at 30 V, and a photocurrent density of 9.35 × 10^{-9} A cm^{-2} under illumination with 266 nm UV light with an irradiance of 0.35 mW cm^{-2}. In terms of Cs$_5$Sb$_2$Cl$_{11}$, the

This journal is © the Partner Organisations 2024

Inorg. Chem. Front., 2024, 11, 589–601 | 595

Fig. 3 Optical properties of as-grown $Cs_3Sb_2Cl_9$ and $Cs_5Sb_2Cl_{11}$ single crystals. (a) Absorbance and transmittance properties of CSC crystals. Black line: absorbance, light violet line: transmittance, line with hollow triangle: $Cs_3Sb_2Cl_9$, line with hollow foursquare: $Cs_5Sb_2Cl_{11}$. (b) The corresponding Tauc plots display the extrapolated optical band gap. (c) and (d) Temperature-dependent PL spectra of CSC crystals with operating temperatures ranging from 10 K to 275 K. λ_{ex} = 266 nm. (e) and (f) Projection mapping of PL spectra in the CSC crystals. (g) and (h) Decay curves and fitting lines of CSC single crystals excited by a 380 nm laser beam. (c), (e) and (g) $Cs_3Sb_2Cl_9$. (d), (f) and (h) $Cs_5Sb_2Cl_{11}$.

596 | *Inorg. Chem. Front.*, 2024, **11**, 589–601

This journal is © the Partner Organisations 2024

Fig. 4 Device performance of $Cs_3Sb_2Cl_9$ single-crystal photodetectors. (a) $I-V$ curves of the detector in the dark and under different irradiation at 266 nm for bias voltages in the range from −30 V to 30 V. The inset is the device structure. (b) Photocurrent density dependence on the power density of the 266 nm laser. (c) Single photocurrent response cycle with light irradiation ON and OFF, showing rise time (21.7 ms) and decay time (104.4 ms) of the photodetector measured at a bias of 30 V and a light intensity of 0.30 mW cm^{-2}. The inset is the time response of the photodetector with a light irradiance of 0.30 mW cm^{-2}. (d) Responsivity of a $Cs_3Sb_2Cl_9$ single-crystal photodetector as a function of wavelength.

lower leakage current density is around 8.86×10^{-11} A cm^{-2} and the photocurrent density is 2.18×10^{-9} A cm^{-2} at −30 V, larger than that of 1.10×10^{-9} A cm^{-2} at 30 V (Fig. S7†). It is worth noting that the photocurrents of the $Cs_3Sb_2Cl_9$ devices are asymmetrical, and the photocurrents at a positive voltage bias at the irradiated crystal plane are significantly larger than those at a negative bias, and this case is the same even after reversing the crystal plane. The non-symmetry photocurrent with a larger photocurrent at a positive bias reflects the characteristics of a hole-determined photocurrent for this metal–semiconductor heterojunction.[25] In contrast, the $Cs_5Sb_2Cl_{11}$ photodetector exhibits a larger photocurrent at a negative voltage, revealing an electron-determined photocurrent. All of the dark current densities of photodetectors are as low as around 90 pA cm^{-2}, which is advantageous for detecting very

weak signals. The ratio of I_{light}/I_{dark} of the $Cs_3Sb_2Cl_9$ device reaches up to two orders of magnitudes, while it is only 24 for the $Cs_5Sb_2Cl_{11}$ sample, implying that $Cs_3Sb_2Cl_9$ is more suitable as a photodetector material, and thus $Cs_3Sb_2Cl_9$ is chosen for further electrical testing.

The relationship between the photocurrent density (J_{ph}) and the irradiance power density (P) can be well fitted by the power law, *i.e.*, $J_{ph} \propto P^{\alpha}$, with an ideal index α of 0.96, as depicted in Fig. 4b. The fitting factor is very close to the ideal value of 1, implying that there is no space-charge limit effect or defect induced recombination.[53,54] The time response behaviors of the as-prepared photodetectors were determined by periodically turning on and off the 266 nm laser beam under ambient conditions at a drain voltage of 30 V, as shown in the inset of Fig. 4c. When the pulsed laser is on, the current curve

This journal is © the Partner Organisations 2024

Inorg. Chem. Front., 2024, **11**, 589–601 | **597**

Table 1 Key performances of the typical lead-free perovskite PDs ever reported

Photodetector	Bandgap (eV)	Voltage (V)	Wavelength of light source (nm)	On–off ratio	Rise time (ms)	Decay time (ms)	Responsivity (A W^{-1})	Ref.
Cs$_3$BiBr$_6$ SC	2.55	6	400	3	50	60	2.5×10^{-5}	55
Cs$_3$Bi$_2$I$_9$ SCTF	2.13	−2	White light	11 000	0.247	0.230	7.2×10^{-3}	57
Cs$_3$Bi$_2$I$_9$ SC	1.96	10	462	1000	—	—	1.1	58
Cs$_3$Bi$_2$I$_9$ SC	1.94	10	420	24	—	—	1.2×10^{-3}	42
Cs$_3$Sb$_2$I$_9$ MP	2.10	1.5	450	105	0.149	0.158	0.446	59
Cs$_3$Sb$_2$I$_{9-x}$Cl$_x$ TF	1.99	0	505	10^6	—	—	0.205	54
Cs$_3$Sb$_2$I$_9$ MP	2.24	1	532	10^4	0.096	0.058	0.01	60
Cs$_3$Sb$_2$Br$_9$ NP	2.65	10	450	—	48	24	3.8	56
Cs$_3$Sb$_2$Br$_9$ SC	2.26	6	480	10^4	0.2	3.0	2.29	53
Cs$_3$Sb$_2$Cl$_9$ NW	3.40	0.9	410	—	130	230	3616	11
Cs$_3$Sb$_2$Cl$_9$ SC	2.86	30	266	103	21.7	104.4	3.95×10^{-5}	This Work

Notes: single crystals (SC), thin films (TF), microcrystals (MC), microplates (MP), nanowires (NW), nanoplates (NP).

rises very sharply and rapidly, and when it is off, the current intensity quickly returns to the normal dark current value. The photodetector shows a good cycling response and repeatability upon multiple switching cycles. Herein, the rise time and decay time of the photodetector are defined as the time taken for the initial current to increase or decrease to 90% of the peak value, respectively. As shown in Fig. 4c, the rise time is 21.7 ms after triggering and the decay time is 104.4 ms after termination of irradiation. The response speed is consistent with the reported lead-free PVK PDs.[11,55,56] Key performance parameters of the typical lead-free PVK PDs reported previously,[11,42,53–60] as well as our Cs$_3$Sb$_2$Cl$_9$ single crystal devices are listed in Table 1. As shown in Table 1, Bi-based single-crystal PDs are more common, while Sb-based PDs are mainly prepared using nanocrystals, nanoplates, nanowires, and thin films, and Sb-based single-crystal PD is less reported. Compared with thin films and nanowires, charge carrier lifetimes in single crystals are longer due to less defects and hence a lower trap-induced recombination rate, while the carriers in single crystals can be smoothly transported through shorter paths, which shortens the transport time and improves the response speed, making single crystals more favorable for preparing PDs.[1] Compared to the Cs$_3$Sb$_2$Cl$_9$ nanowires-based PDs[11] with a rise time of 130 ms and a decay time of 230 ms, the Cs$_3$Sb$_2$Cl$_9$ single-crystal PD exhibits a shorter response time, which is a good demonstration that high-quality single crystals can improve the response speed.

$$R = \frac{I_{\text{light}} - I_{\text{dark}}}{PS}. \tag{3}$$

The responsivity is expressed as eqn (3), where R is the responsivity, I_{light} and I_{dark} are the photocurrent (A) and the dark current (A), respectively, P is the incident light intensity (W cm^{-2}), and S is the effective illuminated area (cm^2). The responsivity of Cs$_3$Sb$_2$Cl$_9$ single crystal PD reaches 3.95×10^{-5} A W^{-1} under 266 nm laser irradiation at 30 V with a low irradiance of 0.005 mW cm^{-2}. The value of responsivity is of the same order of magnitude as the value of 2.5×10^{-5} A W^{-1} for the Cs$_3$BiCl$_6$ single crystal PD at 6 V.[55] Compared to iodine- and bromine-based halide perovskites, the surface states of chlorine-based perovskites are often not so stable and are more susceptible to deterioration under an air atmosphere. This relatively low responsivity may result from severe surface recombination at the interface of the Cs$_3$Sb$_2$Cl$_9$ single crystal and the Au electrode. The spectral responsivity of the photodetector under the ambient environment is shown in Fig. 4d. A very sharp cutoff in the spectral responsivity wavelength can be observed at around 430 nm, corresponding to a photon energy of 2.88 eV. This result agrees well with the absorbance and transmittance spectra of Cs$_3$Sb$_2$Cl$_9$ single crystal shown in Fig. 3a, indicating that the detector has obvious wavelength selectivity and shows good sensitivity to UV light. The UV (360 nm) to visible (480 nm) rejection ratio (R_{360}/R_{480}) is about 150, indicating an intrinsic visible-blind characteristic of the Cs$_3$Sb$_2$Cl$_9$ single crystal UV detector.

Conclusions

In summary, the issue of low solubility of CSC materials has been overcome by using a hybrid solvent consisting of DMSO and hydrochloric acid, and limpid perovskite precursor solutions with high solubility have been successfully prepared. Centimeter-sized high-quality α-Cs$_3$Sb$_2$Cl$_9$ and Cs$_5$Sb$_2$Cl$_{11}$ single crystals have been prepared via the controlled gradient cooling temperature crystallization method using the prepared hybrid solvent. These as-grown single crystals exhibited superior optical and electrical characteristics, and are ideal materials for detecting UV light. The α-Cs$_3$Sb$_2$Cl$_9$ single-crystal photodetector shows a low dark current density of 91 pA cm^{-2} at a bias of 30 V, a high UV/visible rejection ratio of 150, a high photo-to-dark current ratio of two orders of magnitude and a fast response speed with a rise time of 21.7 ms and a decay time of 104.4 ms. All results demonstrate that the α-Cs$_3$Sb$_2$Cl$_9$ single crystal photodetector is a competitive candidate for the application of visible-blind UV detectors. In addition, the successful use of hybrid solvents to enhance solubility suggests the potential for their application to the growth of all chlorine-based perovskite single crystals, thereby facilitating future exploration of these materials in optoelectronic devices.

598 | *Inorg. Chem. Front.*, 2024, **11**, 589–601

This journal is © the Partner Organisations 2024

Author contributions

Conflicts of interest

There are no conflicts to declare.

Acknowledgements

References

1 G. Maculan, A. D. Sheikh, A. L. Abdelhady, M. I. Saidaminov, M. A. Haque, B. Murali, E. Alarousu, O. F. Mohammed, T. Wu and O. M. Bakr, $CH_3NH_3PbCl_3$ Single Crystals: Inverse Temperature Crystallization and Visible-Blind UV-Photodetector, *J. Phys. Chem. Lett.*, 2015, **6**, 3781–3786.

2 H. Wei, Y. Fang, P. Mulligan, W. Chuirazzi, H.-H. Fang, C. Wang, B. R. Ecker, Y. Gao, M. A. Loi, L. Cao and J. Huang, Sensitive X-ray detectors made of methylammonium lead tribromide perovskite single crystals, *Nat. Photonics*, 2016, **10**, 333–339.

3 M. I. Saidaminov, M. A. Haque, J. Almutlaq, S. Sarmah, X.-H. Miao, R. Begum, A. A. Zhumekenov, I. Dursun, N. Cho, B. Murali, O. F. Mohammed, T. Wu and O. M. Bakr, Inorganic Lead Halide Perovskite Single Crystals: Phase-Selective Low-Temperature Growth, Carrier Transport Properties, and Self-Powered Photodetection, *Adv. Opt. Mater.*, 2017, **5**, 1600704.

4 B. Zhou, D. Ding, Y. Wang, S. Fang, Z. Liu, J. Tang, H. Li, H. Zhong, B. Tian and Y. Shi, A Scalable H_2O–DMF–DMSO Solvent Synthesis of Highly Luminescent Inorganic Perovskite–Related Cesium Lead Bromides, *Adv. Opt. Mater.*, 2021, **9**, 2001435.

5 M. Deng, Z. Li, X. Deng, Y. Hu and X. Fang, Wafer-scale heterogeneous integration of self-powered lead-free metal halide UV photodetectors with ultrahigh stability and homogeneity, *J. Mater. Sci. Technol.*, 2023, **164**, 150–159.

6 Z. Li, T. Yan and X. Fang, Low-dimensional wide-bandgap semiconductors for UV photodetectors, *Nat. Rev. Mater.*, 2023, **8**, 587–603.

7 P. Gui, H. Zhou, F. Yao, Z. Song, B. Li and G. Fang, Space–Confined Growth of Individual Wide Bandgap Single Crystal $CsPbCl_3$ Microplatelet for Near–Ultraviolet Photodetection, *Small*, 2019, **15**, 1902618.

8 J. Dziedzic, J. Mróz and R. Jakubas, Pyroelectric and dilatometric studies on the low temperature ferroelectric phase transition of $(CH_3NH_3)_5Bi_2Br_{11}$, *Acta Phys. Pol., A*, 2005, **108**, 505–511.

9 C. Wu, Q. Zhang, G. Liu, Z. Zhang, D. Wang, B. Qu, Z. Chen and L. Xiao, From Pb to Bi: A Promising Family of Pb–Free Optoelectronic Materials and Devices, *Adv. Energy Mater.*, 2019, **10**, 1902496.

10 K. Kihara and T. Sudo, Two structure types of cesium antimony nonachloride, $Cs_3Sb_2Cl_9$, *Z. Kristallogr.*, 1971, **134**, 155–158.

11 B. Pradhan, G. S. Kumar, S. Sain, A. Dalui, U. K. Ghorai, S. K. Pradhan and S. Acharya, Size Tunable Cesium Antimony Chloride Perovskite Nanowires and Nanorods, *Chem. Mater.*, 2018, **30**, 2135–2142.

12 A. Pradhan, S. C. Sahoo, A. K. Sahu and S. L. Samal, Effect of Bi Substitution on $Cs_3Sb_2Cl_9$: Structural Phase Transition and Band Gap Engineering, *Cryst. Growth Des.*, 2020, **20**, 3386–3395.

13 A. Singh, N. C. Chiu, K. M. Boopathi, Y. J. Lu, A. Mohapatra, G. Li, Y. F. Chen, T. F. Guo and C. W. Chu, Lead-Free Antimony-Based Light-Emitting Diodes through the Vapor-Anion-Exchange Method, *ACS Appl. Mater. Interfaces*, 2019, **11**, 35088–35094.

14 X. Wang, N. Ali, G. Bi, Y. Wang, Q. Shen, A. Rahimi-Iman and H. Wu, Lead-Free Antimony Halide Perovskite with Heterovalent Mn^{2+} Doping, *Inorg. Chem.*, 2020, **59**, 15289–15294.

15 B. Ptaszyński, Thermoanalytical studies of compounds of general formula $Cs_3[Sb_xBi_{2-x}Cl_9]$, *Thermochim. Acta*, 1987, **116**, 225–233.

16 B. Ptaszyński, A study of thermal decomposition of complex compounds of $Cs_3[Sb_{2-x}Pb_xCl_{9-x}]$ type, *Thermochim. Acta*, 1988, **130**, 299–307.

17 G. Kresse and J. Furthmüller, Efficient iterative schemes for ab initio total-energy calculations using a plane-wave basis set, *Phys. Rev. B: Condens. Matter Mater. Phys.*, 1996, **54**, 11169–11186.

18 C. Freysoldt, B. Grabowski, T. Hickel, J. Neugebauer, G. Kresse, A. Janotti and C. G. Van de Walle, First-principles calculations for point defects in solids, *Rev. Mod. Phys.*, 2014, **86**, 253–305.

19 R. P. Oertel, Vibrational spectra of dimethyl sulfoxide complexes of antimony(III) and bismuth(III) halides, *Spectrochim. Acta, Part A*, 1970, **26**, 659–669.

20 J. C. Hamill, J. Schwartz and Y.-L. Loo, Influence of Solvent Coordination on Hybrid Organic–Inorganic Perovskite Formation, *ACS Energy Lett.*, 2017, **3**, 92–97.

21 P. K. Nayak, D. T. Moore, B. Wenger, S. Nayak, A. A. Haghighirad, A. Fineberg, N. K. Noel, O. G. Reid,

This journal is © the Partner Organisations 2024

Inorg. Chem. Front., 2024, **11**, 589–601 | **599**

G. Rumbles, P. Kukura, K. A. Vincent and H. J. Snaith, Mechanism for rapid growth of organic-inorganic halide perovskite crystals, *Nat. Commun.*, 2016, **7**, 13303.

22 M. A. Flatken, E. Radicchi, R. Wendt, A. G. Buzanich, E. Härk, J. Pascual, F. Mathies, O. Shargaieva, A. Prause, A. Dallmann, F. De Angelis, A. Hoell and A. Abate, Role of the Alkali Metal Cation in the Early Stages of Crystallization of Halide Perovskites, *Chem. Mater.*, 2022, **34**, 1121–1131.

23 M. Fontana, G. Maisano, P. Migliardo, C. Vasi and F. Wanderlingh, Raman Scattering and Melting Point in $SbCl_3$, *Optica Acta: Int J Opt*, 1980, **27**, 1087–1093.

24 J. Milne, Spectrophotometric Studies on Sb(III) in Hydrochloric Acid Solutions, *Can. J. Chem.*, 1975, **53**, 888–893.

25 W. Wang, H. Meng, H. Qi, H. Xu, W. Du, Y. Yang, Y. Yi, S. Jing, S. Xu, F. Hong, J. Qin, J. Huang, Z. Xu, Y. Zhu, R. Xu, J. Lai, F. Xu, L. Wang and J. Zhu, Electronic-Grade High-Quality Perovskite Single Crystals by a Steady Self-Supply Solution Growth for High-Performance X-ray Detectors, *Adv. Mater.*, 2020, **32**, 2001540.

26 B. Vargas, E. Ramos, E. Pérez-Gutiérrez, J. C. Alonso and D. Solis-Ibarra, A Direct Bandgap Copper−Antimony Halide Perovskite, *J. Am. Chem. Soc.*, 2017, **139**, 9116–9119.

27 B. Saparov, F. Hong, J.-P. Sun, H.-S. Duan, W. Meng, S. Cameron, I. G. Hill, Y. Yan and D. B. Mitzi, Thin-Film Preparation and Characterization of $Cs_3Sb_2I_9$: A Lead-Free Layered Perovskite Semiconductor, *Chem. Mater.*, 2015, **27**, 5622–5632.

28 P. E. Tomaszewski, Crystal Structure and Phase Transitions in the $A_3B_2X_9$ Family of Crystals, *Phys. Status Solidi B*, 1994, **181**, 15–21.

29 R. Jakubas, A new ferroelectric compound $(CH_3NH_3)_5Bi_2Br_{11}$, *Solid State Commun.*, 1989, **69**, 267–269.

30 R. Jakubas, L. Sobczyk and J. Lefebvre, A new ferroelectric crystal $(CH_3NH_3)_5Bi_2Cl_{11}$, *Ferroelectrics*, 1989, **100**, 143–149.

31 J. Mróz and R. Jakubas, Ferroelectricity in $(CH_3NH_3)_5Bi_2Br_{11}$ crystals, *Solid State Commun.*, 1989, **72**, 813–816.

32 J. Lefebvre, P. Carpentier and R. Jakubas, Structures and phase transition in the ferroelectric crystal of pentakis (methylammonium) undecachlorodibismuthate(III) $[NH_3(CH_3)]_5Bi_2Cl_{11}$, *Acta Crystallogr., Sect. B: Struct. Sci.*, 1991, **47**, 228–234.

33 Y. Liu, Y. Zhang, Z. Yang, J. Feng, Z. Xu, Q. Li, M. Hu, H. Ye, X. Zhang, M. Liu, K. Zhao and S. Liu, Low-temperature-gradient crystallization for multi-inch high-quality perovskite single crystals for record performance photodetectors, *Mater. Today*, 2019, **22**, 67–75.

34 B. Su, M. Li, E. Song and Z. Xia, Sb^{3+} Doping in Cesium Zinc Halides Single Crystals Enabling High–Efficiency Near–Infrared Emission, *Adv. Funct. Mater.*, 2021, **31**, 2105316.

35 R. Xu, Z. Hong, X. Tong, W. Wang, H. Meng, J. Qin, X. Wang, X. Shu, J. Cai, Z. Zhang, F. Xu, H. Xu, F. Hong, H. Qi, J. Lai and D. Li, Uncovering the Formation Mechanism of Striations and Pyramidal Pits on a Native $MAPbI_3$ Single-Crystal Surface, *J. Phys. Chem. C*, 2022, **126**, 7319–7325.

36 Y. Yuan, R. Xu, H. Xu, F. Hong, F. Xu and L. Wang, Nature of the band gap of halide perovskites ABX_3 (A = CH_3NH_3, Cs; B = Sn, Pb; X = Cl, Br, I): First-principles calculations, *Chin. Phys. B*, 2015, **24**, 116302.

37 D. O. Scanlon, C. W. Dunnill, J. Buckeridge, S. A. Shevlin, A. J. Logsdail, S. M. Woodley, C. R. Catlow, M. J. Powell, R. G. Palgrave, I. P. Parkin, G. W. Watson, T. W. Keal, P. Sherwood, A. Walsh and A. A. Sokol, Band alignment of rutile and anatase TiO_2, *Nat. Mater.*, 2013, **12**, 798–801.

38 Z. Yang, W. Meng, J. Kang, X. Wang, X. Shu, T. Chen, R. Xu, F. Xu and F. Hong, Unraveling the Defect-Dominated Broadband Emission Mechanisms in (001)-Preferred Two-Dimensional Layered Antimony-Halide Perovskite Film, *J. Phys. Chem. Lett.*, 2022, **13**, 11736–11744.

39 K. M. McCall, Z. Liu, G. Trimarchi, C. C. Stoumpos, W. Lin, Y. He, I. Hadar, M. G. Kanatzidis and B. W. Wessels, α-Particle Detection and Charge Transport Characteristics in the $A_3M_2I_9$ Defect Perovskites (A = Cs, Rb; M = Bi, Sb), *ACS Photonics*, 2018, **5**, 3748–3762.

40 L. Zhou, J. Liao, Z. Huang, J. Wei, X. Wang, H. Chen and D. Kuang, Intrinsic Self-Trapped Emission in 0D Lead-Free $(C_4H_{14}N_2)_2In_2Br_{10}$ Single Crystal, *Angew. Chem., Int. Ed.*, 2019, **58**, 15435–15440.

41 X. Li, X. Du, P. Zhang, Y. Hua, L. Liu, G. Niu, G. Zhang, J. Tang and X. Tao, Lead-free halide perovskite $Cs_3Bi_2Br_9$ single crystals for high-performance X-ray detection, *Sci. China Mater.*, 2021, **64**, 1427–1436.

42 H. Zhang, Y. Xu, Q. Sun, J. Dong, Y. Lu, B. Zhang and W. Jie, Lead free halide perovskite $Cs_3Bi_2I_9$ bulk crystals grown by a low temperature solution method, *CrystEngComm*, 2018, **20**, 4935–4941.

43 H. Li, J. Song, W. Pan, D. Xu, W. Zhu, H. Wei and B. Yang, Sensitive and Stable 2D Perovskite Single-Crystal X-ray Detectors Enabled by a Supramolecular Anchor, *Adv. Mater.*, 2020, **32**, 2003790.

44 A. Ciżman, R. Poprawski and A. Sieradzki, Ferroelectric phase transition in $(CH_3NH_3)_5Bi_2Cl_{11}$ and $(CH_3NH_3)_5Bi_2Br_{11}$ crystals, *Phase Transitions*, 2007, **80**, 171–176.

45 J. Tauc, R. Grigorovici and A. Vancu, Optical Properties and Electronic Structure of Amorphous Germanium, *Phys. Status Solidi B*, 1966, **15**, 627–637.

46 J. Luo, X. Wang, S. Li, J. Liu, Y. Guo, G. Niu, L. Yao, Y. Fu, L. Gao, Q. Dong, C. Zhao, M. Leng, F. Ma, W. Liang, L. Wang, S. Jin, J. Han, L. Zhang, J. Etheridge, J. Wang, Y. Yan, E. H. Sargent and J. Tang, Efficient and stable emission of warm-white light from lead-free halide double perovskites, *Nature*, 2018, **563**, 541–545.

47 S. Li, J. Luo, J. Liu and J. Tang, Self-Trapped Excitons in All-Inorganic Halide Perovskites: Fundamentals, Status, and Potential Applications, *J. Phys. Chem. Lett.*, 2019, **10**, 1999–2007.

48 H.-H. Fang, S. Adjokatse, H. Wei, J. Yang, G. R. Blake, J. Huang, J. Even and M. A. Loi, Ultrahigh sensitivity of

600 | *Inorg. Chem. Front.*, 2024, **11**, 589–601

This journal is © the Partner Organisations 2024

methylammonium lead tribromide perovskite single crystals to environmental gases, *Mat. Sci.*, 2016, **2**, 1–9.

49 D. Shi, V. Adinolfi, R. Comin, M. Yuan, E. Alarousu, A. Buin, Y. Chen, S. Hoogland, A. Rothenberger, K. Katsiev, Y. Losovyj, X. Zhang, P. A. Dowben, O. F. Mohammed, E. H. Sargent and O. M. Bakr, Low trap-state density and long carrier diffusion in organolead trihalide perovskite single crystals, *Science*, 2015, **347**, 519–522.

50 Y. Jiang, M. Cui, S. Li, C. Qin, Y. Liu and M. Yuan, Reducing the impact of Auger recombination in quasi-2D perovskite light-emitting diodes, *Nat. Commun.*, 2021, **12**, 1–10.

51 M. Keshavarz, E. Debroye, M. Ottesen, C. Martin, H. Zhang, E. Fron, R. Kuchler, J. A. Steele, M. Bremholm, J. Van de Vondel, H. I. Wang, M. Bonn, M. B. J. Roeffaers, S. Wiedmann and J. Hofkens, Tuning the Structural and Optoelectronic Properties of $Cs_2AgBiBr_6$ Double-Perovskite Single Crystals through Alkali-Metal Substitution, *Adv. Mater.*, 2020, **32**, 2001878.

52 Y. Feng, L. Pan, H. Wei, Y. Liu, Z. Ni, J. Zhao, P. N. Rudd, L. R. Cao and J. Huang, Low defects density $CsPbBr_3$ single crystals grown by an additive assisted method for gamma-ray detection, *J. Mater. Chem. C*, 2020, **8**, 11360–11368.

53 P. Liu, Y. Liu, S. Zhang, J. Li, C. Wang, C. Zhao, P. Nie, Y. Dong, X. Zhang, S. Zhao and G. Wei, Lead–Free $Cs_3Sb_2Br_9$ Single Crystals for High Performance Narrowband Photodetector, *Adv. Opt. Mater.*, 2020, **8**, 2001072.

54 J. Mei, M. Liu, P. Vivo and V. Pecunia, Two–Dimensional Antimony–Based Perovskite–Inspired Materials for High–Performance Self–Powered Photodetectors, *Adv. Funct. Mater.*, 2021, **31**, 2106295.

55 Y. Tang, M. Liang, B. Chang, H. Sun, K. Zheng, T. Pullerits and Q. Chi, Lead-free double halide perovskite Cs_3BiBr_6 with well-defined crystal structure and high thermal stability for optoelectronics, *J. Mater. Chem. C*, 2019, **7**, 3369–3374.

56 Z. Zheng, Q. Hu, H. Zhou, P. Luo, A. Nie, H. Zhu, L. Gan, F. Zhuge, Y. Ma, H. Song and T. Zhai, Submillimeter and lead-free $Cs_3Sb_2Br_9$ perovskite nanoflakes: inverse temperature crystallization growth and application for ultra-sensitive photodetectors, *Nanoscale Horiz.*, 2019, **4**, 1372–1379.

57 W. G. Li, X. D. Wang, J. F. Liao, Y. Jiang and D. B. Kuang, Enhanced On–Off Ratio Photodetectors Based on Lead–Free $Cs_3Bi_2I_9$ Single Crystal Thin Films, *Adv. Funct. Mater.*, 2020, **30**, 1909701.

58 Y. Zhang, Y. Liu, Z. Xu, H. Ye, Z. Yang, J. You, M. Liu, Y. He, M. G. Kanatzidis and S. F. Liu, Nucleation-controlled growth of superior lead-free perovskite $Cs_3Bi_2I_9$ single-crystals for high-performance X-ray detection, *Nat. Commun.*, 2020, **11**, 2304.

59 Z. Lai, Y. Meng, F. Wang, X. Bu, W. Wang, P. Xie, W. Wang, C. Liu, S. Yip and J. C. Ho, Direct drop-casting synthesis of all-inorganic lead and lead-free halide perovskite micro-crystals for high-performance photodetectors, *Nano Res.*, 2021, **15**, 3621–3627.

60 S. K. Shil, F. Wang, Z. Lai, Y. Meng, Y. Wang, D. Zhao, M. K. Hossain, K. O. Egbo, Y. Wang, K. M. Yu and J. C. Ho, Crystalline all-inorganic lead-free $Cs_3Sb_2I_9$ perovskite microplates with ultra-fast photoconductive response and robust thermal stability, *Nano Res.*, 2021, **14**, 4116–4124.

This journal is © the Partner Organisations 2024

Inorg. Chem. Front., 2024, **11**, 589–601 | **601**